Journal of Power Sources 195 (2010) 4984–4989

Contents lists available at ScienceDirect

Journal of Power Sources

journal homepage: www.elsevier.com/locate/jpowsour

Preparation of Li_2S–$GeSe_2$–P_2S_5 electrolytes by a single step ball milling for all-solid-state lithium secondary batteries

James E. Trevey, Yoon Seok Jung[1], Se-Hee Lee*

Department of Mechanical Engineering, University of Colorado at Boulder, Boulder, CO 80309-0427, USA

ARTICLE INFO

Article history:
Received 12 January 2010
Received in revised form 16 February 2010
Accepted 16 February 2010
Available online 20 February 2010

Keywords:
Lithium battery
Solid-state battery
Solid electrolyte
Sulfide
Selenide

ABSTRACT

Glass–ceramic and glass Li_2S–$GeSe_2$–P_2S_5 electrolytes were prepared by a single step ball milling (SSBM) process. Various compositions of $Li_{4-x}Ge_{1-x}P_xS_{2(1+x)}Se_{2(1-x)}$ with/without heat treatment (HT) from $x = 0.55$ to $x = 1.00$ were systematically investigated. Structural analysis by X-ray diffraction (XRD) showed gradual increase of the lattice constant followed by significant phase change with increasing $GeSe_2$. HT also affected the crystallinity. Incorporation of $GeSe_2$ in Li_2S–P_2S_5 kept high conductivity with a maximum value of 1.4×10^{-3} S cm^{-1} at room temperature for $x = 0.95$ in $Li_{4-x}Ge_{1-x}P_xS_{2(1+x)}Se_{2(1-x)}$ without HT. All-solid-state $LiCoO_2$/Li cells using Li_2S–$GeSe_2$–P_2S_5 as solid-state electrolytes (SE) were tested by constant-current constant-voltage (CCCV) charge–discharge cycling at a current density of 50 μA cm^{-2} between 2.5 and 4.3 V (*vs.* Li/Li$^+$). In spite of the extremely high conductivity of the SE, $LiCoO_2$/Li cells showed a large irreversible reaction especially during the first charging cycle. $LiCoO_2$ with SEs heat-treated at elevated temperature exhibited a capacity over 100 mAh g^{-1} at the second cycle and consistently improved cycle retention, which is believed to be due to the better interfacial stability.

1. Introduction

Research on all-solid-state rechargeable lithium-ion batteries has increased considerably in recent years due to raised concerns relating to safety hazards such as solvent leakage and flammability of liquid electrolytes used for commercial lithium-ion batteries [1–7]. Due to the increased level of safety that SEs offer [8,9] an extensive global effort is under way to produce a viable SE to replace conventional liquid electrolytes. Beyond the safety advantage, all-solid-state batteries maintain a high degree of reliability, can vary in form and design, and can be constructed with a wide variety of SE materials [4,10–12]. Unfortunately research has yet to unveil a SE that can outperform liquid electrolyte. Inferior rate capability, low ionic conductivity, interfacial instability, and low loading of active materials are just a few of the barriers that stand in the way of the commercialization of all-solid-state rechargeable lithium-ion batteries [4,5]. Ideally, liquid electrolytes could be replaced by SEs that perform similarly without excessive safety issues in the future [13].

While melt and quench methods have produced promising results in the past, ball milling has emerged as a more enticing method for SE development because it is relatively low cost and less time consuming [14]. Conventional ball milling techniques have proven useful for generating ultra-fine amorphous materials at room temperature. Fine powders function well for achieving high ionic conductivities as well as close contact between electrolytes and electrode materials for all-solid-state cells [1,2]. Ball milling has also proven effective for enlarging the compositional region in which amorphous materials are obtained, beyond that of conventional melt-quenching methods [7,15]. Ball milled amorphous powders are often heat-treated to attain a crystalline structure capable of even higher conductivities than those reached by amorphous powders. HT of glass samples to a crystalline glass–ceramic state has shown to increase conductivity among Li_2S–P_2S_5 glass SEs, which is attributed to the precipitation of highly lithium-ion-conducting crystals [11,16,17].

All-solid-state batteries with sulfide SEs are very promising due to high conductivities and wide electrochemical windows [18]. Ionic conductivity of sulfide electrolytes can be improved by increasing the Li_2S content in glasses or by adding a second network-forming sulfide. Increasing the Li_2S content increases the carrier ion concentration thereby enhancing the ionic conductivity of lithium ions but results in higher instability against crystallization, which limits the glass-forming region. The addition of a second network former to ion-conducting glasses has reported to cause an enhancement of ion conductivities, called the "mixed-anion effect" [15].

By adding second network formers such as GeS_2 and SiS_2 to the Li_2S–P_2S_5 system in previous works, researchers have obtained

* Corresponding author. Tel.: +1 303 492 7889; fax: +1 303 492 3498.
E-mail address: sehee.lee@colorado.edu (S.-H. Lee).
[1] Present address: National Renewable Energy Laboratory, Golden, CO 80401, USA.

0378-7753/$ – see front matter © 2010 Elsevier B.V. All rights reserved.
doi:10.1016/j.jpowsour.2010.02.042

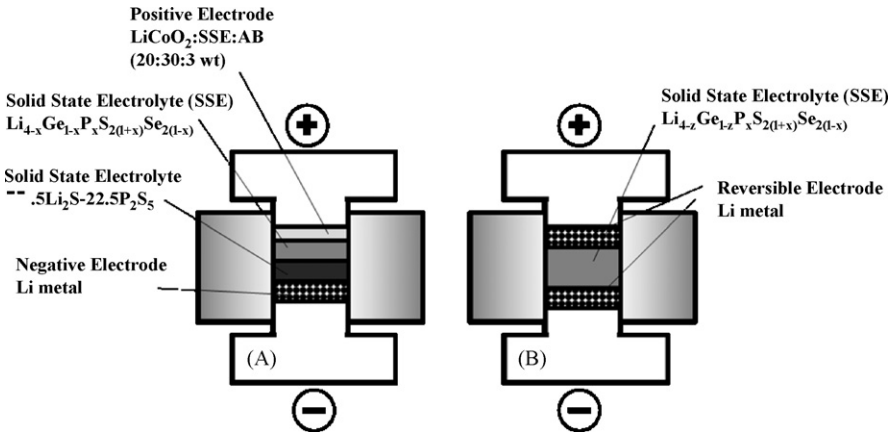

Fig. 1. Schematic diagram of Ti test die for (a) the all-solid-state battery and (b) measuring conductivity of SE.

higher conductivities for solid electrolytes. These second network formers maintain elements with large ionic radii and high polarizability, that allow for enhancement of mobility of conducting ions. Motivated by larger ionic size and more polarizability of selenium than sulfur, which could lead to increase of conductivity, we report on the inclusion of $GeSe_2$ as the second network former into the Li_2S–P_2S_5 system which showed great improvement of ionic conductivity. We attribute the conductivity improvement to the large ionic radius of Ge and Se and the more polarizable character of Se ions improving the mobility of the conducting species [19]. All-solid-state cells were constructed using $LiCoO_2$ as a cathode material, Li_2S–$GeSe_2$–P_2S_5 as a SE. The effects of HT on the electrochemical performance of Li/$LiCoO_2$ cells were evaluated.

2. Experimental

Li_2S–$GeSe_2$–P_2S_5 ($Li_{4-x}Ge_{1-x}P_xS_{2(1+x)}Se_{2(1-x)}$) electrolytes were prepared by SSBM with/without HT [20]. Reagent-grade powders of Li_2S (Aldrich, 99.999%), P_2S_5 (Aldrich, 99%), and $GeSe_2$ (Strem, 99.999%) were used as starting materials. Appropriate concentrations of materials were combined into a zirconia vial (Spex) at a net weight of 1 g with two zirconia balls (1 × 12 mm, 1 × 15 mm in diameter) for grinding. High energy ball milling (Spex8000) took place for 20 continuous hours in an Ar-filled dry box. HT for as-ball-milled (ABM) SE powders were performed by first pelletizing the powders at 8 metric tons in a stainless steel die (ϕ = 1.3 cm) with 400 mg of starting material. Extracted pellets were placed in a sealed glass container and heated on a hot plate to the desired temperature at approximately 10 °C min^{-1}. With the starting time corresponding to the point when the hot plate reached the desired temperature, finished pellets were removed from the hot plate and placed on a cooling rack. The post-heat-treated (PHT) pellets were then ground in a mortar with pestle.

Composite electrodes were prepared by mixing $LiCoO_2$ powder (Sigma–Aldrich), SE Li_2S–$GeSe_2$–P_2S_5, and acetylene black (Alfa-Aesar, 50% compressed) at a weight ratio of 20:30:3 respectively. Bilayer electrolyte pellets are formed by hand pressing 100 mg of Li_2S–$GeSe_2$–P_2S_5 SE on top of a 100 mg hand pressed layer of 77.5Li_2S–22.5P_2S_5 (mol%) SE prepared by the SSBM procedure. We used this bilayer SE with 77.5Li_2S–22.5P_2S_5 (mol%) on Li metal side as can be seen in Fig. 1(a) since this 77.5Li_2S–22.5P_2S_5 (mol%) SE was demonstrated to be stable against Li metal [20]. A 10 mg layer of the composite cathode material is then carefully spread on the top of the Li_2S–$GeSe_2$–P_2S_5 electrolyte layer and the cell pelletized by cold pressing (5 metric tons) for 5 min. Li foil (Alfa-Aesar, 0.75 mm thick) is then attached to the 77.5Li_2S–22.5P_2S_5 (mol%) SE face at 2 metric tons. All pressing and testing operations are carried out in a polyaryletheretherketone (PEEK) mold (ϕ = 1.3 cm) with Ti metal rods as current collectors for both working and counter electrodes. All processes were carried out in an Ar-filled glove box. Galvanostatic charge-discharge cycling took place at first cycle cut off voltages of 4.1 and 2.5 V while the remaining cycles were run from 2.5 to 4.3 V at a current of 50 μA cm^{-2} at room temperature using Arbin BT2000.

SE samples were characterized by XRD measurement with Cu Kα radiation. Samples were sealed in an airtight aluminum container with beryllium windows and mounted on the X-ray diffractometer (PANalytical, PW3830). Ionic conductivities were measured by AC impedance spectroscopy (Solartron 1280C). Weighed materials are cold pressed at 5 metric tons, before lithium metal plates are pressed to both sides of the pellet at 1 metric ton to serve as electrodes. The impedance of selected cells was measured from 20 MHz to 100 mHz at room temperature and the conductivity was determined using complex impedance analysis. Schematic diagrams for the Li/SE/$LiCoO_2$ cells and AC impedance cells can be seen in Fig. 1(a) and (b), respectively.

3. Results and discussion

A schematic diagram for ternary component Li_2S–$GeSe_2$–P_2S_5 is shown in Fig. 2. As x in $Li_{4-x}Ge_{1-x}P_xS_{2(1+x)}Se_{2(1-x)}$ increases, $GeSe_2$ decreases and P_2S_5 increases with relatively small changes of Li_2S, and finally x = 1.00 corresponds with 75Li_2S–25P_2S_5 (mol%).

Fig. 3(a) shows the recorded conductivities of the $Li_{4-x}Ge_{1-x}P_xS_{2(1+x)}Se_{2(1-x)}$ in the range of $0.55 < x < 1.00$. Relatively high conductivities were observed for the entire range of compositions with values ranging from 5.1×10^{-4} S cm^{-1} at the lowest and 1.4×10^{-3} S cm^{-1} at the highest but with most values recording above 1×10^{-3} S cm^{-1} as shown in Table 1. We observed a typical activation energy of 30–32 kJ mol^{-1} over the entire compositional range following plot of the Arrhenius equation where

Table 1
Conductivity of $Li_{4-x}Ge_{1-x}P_{2(1+x)}S_{2(1-x)}$.

x	Conductivity/S cm^{-1}
0.55	9.8×10^{-4}
0.60	1.2×10^{-3}
0.65	1.2×10^{-3}
0.70	1.4×10^{-3}
0.75	5.1×10^{-4}
0.80	1.1×10^{-3}
0.85	8.2×10^{-4}
0.90	1.2×10^{-3}
0.95	1.4×10^{-3}
1.00	9.4×10^{-4}

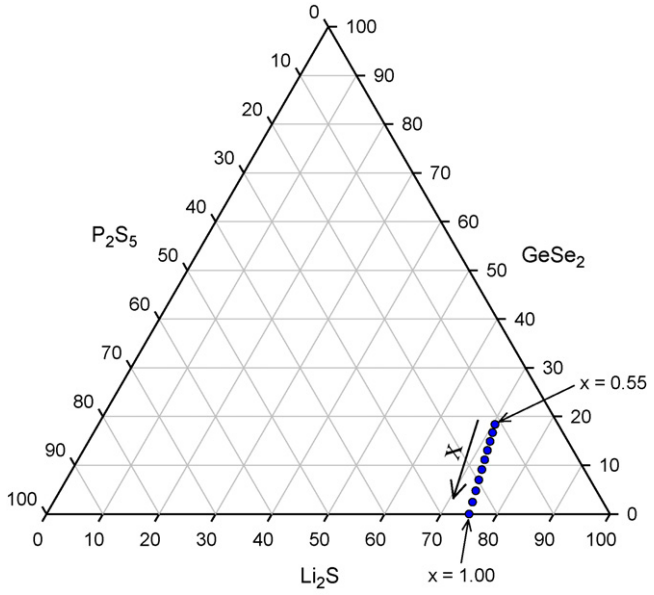

Fig. 2. Diagram for ternary components of Li_2S–$GeSe_2$–P_2S_5 which is also expressed as $Li_{4-x}Ge_{1-x}P_xS_{2(1+x)}Se_{2(1-x)}$.

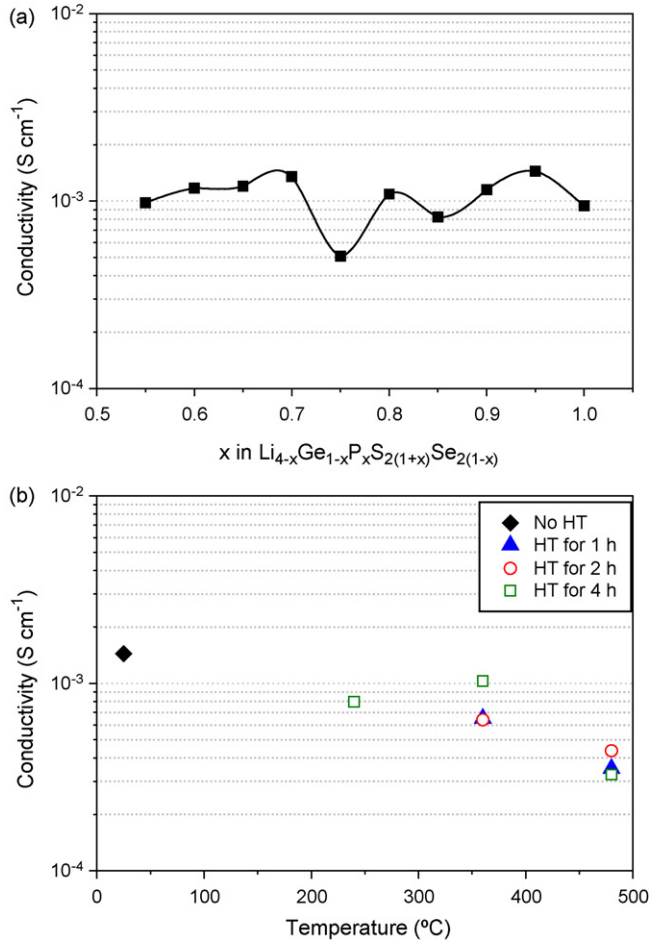

Fig. 3. (a) Electrical conductivity of ABM for $Li_{4-x}Ge_{1-x}P_xS_{2(1+x)}Se_{2(1-x)}$. (b) Conductivity map of PHT series for $Li_{4-x}Ge_{1-x}P_xS_{2(1+x)}Se_{2(1-x)}$ with $x = 0.95$.

Table 2
Conductivity of $Li_{4-x}Ge_{1-x}P_{2(1+x)}S_{2(1-x)}$ with $x = 0.95$.

Heat treatment		Conductivity/S cm^{-1}
Temperature/°C	Time/h	
ABM		1.4×10^{-3}
240	4	8.0×10^{-4}
360	1	6.5×10^{-4}
360	2	6.4×10^{-4}
360	4	1.0×10^{-3}
480	1	3.5×10^{-4}
480	2	4.4×10^{-4}
480	4	3.3×10^{-4}

the slope of [Ln(σ) vs. $1/T$] is equal to ($-E_a/R$). Here σ is the conductivity, T is the absolute temperature, E_a the activation energy for conduction, and R is the gas constant [1,11]. Comparatively, typical values for activation energy for similar systems include 35–40 kJ mol^{-1} for Li_2S–GeS_2–P_2S_5 [15] and 35–45 kJ mol^{-1} for Li_2S–P_2S_5 [21], which places our SE among some of the best thus far. The highest recorded value for conductivity corresponds to the composition of $x = 0.95$, which relates to the molar compositions of constituent compounds as $74.4Li_2S$–$2.4GeSe_2$–$23.2P_2S_5$ (mol%). This composition is closely related to that of the highest recorded conductivity for the Li_2S–GeS_2–P_2S_5 system studied by Yamamoto group [15]. We attribute the high ionic conductivities of this system to the mixed-anion effect which involved the mixing of two kinds of network-forming sulfides P_2S_5 and $GeSe_2$, and the presence of a large concentration of Li in the glass and glass–ceramic materials [15]. The high ionic conductivities may also be due to the larger ionic radii of Ge and Se atoms which improve the mobility of the conducting species [19]. As we received our highest conductivity from the composition $x = 0.95$, we used this material exclusively for PHT studies. Other compositions were initially considered and tested but did not yield significantly comparable results to that of $x = 0.95$, which proved to be optimal for our research.

Fig. 3(b) shows a conductivity map for all PHT samples. A trend of decreasing conductivity with increased PHT temperature is observed among all samples. ABM powder was heat-treated to seven different conditions specified in Table 2 with corresponding recorded conductivities. Data were taken for 1, 2, and 4 h to observe the effects of time on conductivity and crystal structure. PHT time variation showed slight changes in conductivity. A single 4-h measurement is shown for the sample heated to 240 °C due to insignificant changes from the ABM starting material conductivity. For samples heat-treated to 360 and 480 °C we observe similar traits for the different HT times with one exception. Comparison of the 1 h HT, 2 and 4 h HTs shows slight variation of conductivities respectively with the exclusion of the sample heat-treated to 360 °C for 4 h reaching a high ionic conductivity above 1.0×10^{-3} S cm^{-1}. The overall trend of decreasing conductivity with higher HT temperatures disagrees with the generally observed behavior of the Li_2S–P_2S_5 system which shows a trend of increasing conductivity. Though, with the exception of the Li_2S–P_2S_5 system, generally crystallization of glassy materials results in lower ionic conductivity [21–24].

The small amount of $GeSe_2$ that is added to the Li_2S–P_2S_5 system has a significant effect on the conductivity and the behavior under HT conditions. The chemical composition dependence on concentration of $GeSe_2$ yields a non-significant change in the amount of Li_2S and instead, $GeSe_2$ essentially replaces P_2S_5 (Fig. 2). Because the conductivity of Li^+ ion-conducting materials is known to be determined mainly by the lithium concentration in the glasses [14], and we have a somewhat unwavering amount of Li contribution from the Li_2S, we observe only small changes in the high conductivity of the Li_2S–GeS_2–P_2S_5 system over its wide compositional

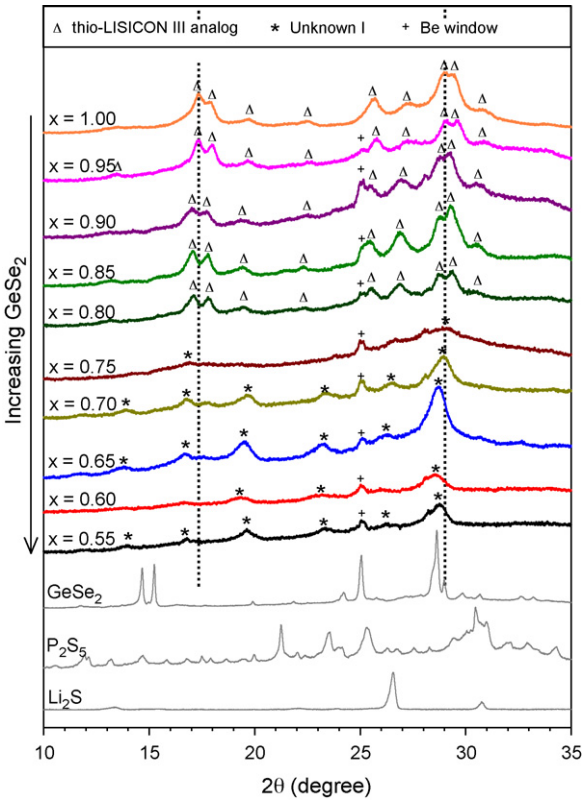

Fig. 4. XRD patterns of ABM for $Li_{4-x}Ge_{1-x}P_xS_{2(1+x)}Se_{2(1-x)}$. XRD patterns for the precursor powders (Li_2S, P_2S_5, and $GeSe_2$) are shown for comparison.

region. We achieved high ionic conductivities for both ABM material with varying chemical compositions and PHT material with varying temperatures and times.

In order to show the dominant trends among the compositional range of ball milled materials, XRD patterns of the $Li_{4-x}Ge_{1-x}P_xS_{2(1+x)}Se_{2(1-x)}$ powders for $0.55 < x < 1.00$ without HT are shown in Fig. 4. Several interesting trends are observed over the large range of tested compositions. Foremost the gradual negative shift of the "thio-LISICON III analog" peaks (triangle) starting from $x = 1.00$ and ending at $x = 0.75$ is noticeable. This could be explained by larger ionic size of Ge and Se, which can enlarge the whole Li_2S–P_2S_5 lattice. In spite of two exceptions for $x = 0.75$ and 0.85, one of the reasons for slightly increased conductivity by adding $GeSe_2$ might be more open structure for better Li^+ transport than Li_2S–P_2S_5 system ($x = 1.00$). With further decreasing x we observe a totally different crystalline structure for ABM materials ('*') from that of Li_2S–P_2S_5 compounds. Surprisingly, the new structure represents even higher conductivities than Li_2S–P_2S_5 system ($x = 1.00$) (Table 1). The most interesting point, however, is the close correlation that can be drawn between the changing crystal structures, and the variations in ionic conductivity. The composition with the lowest conductivity among the tested compositions corresponded to the only amorphous phase of material which also represents a turning point for large overall changes in the dominant crystal structure.

XRD patterns of heat-treated samples are shown in Fig. 5 where we see the progression of ABM material go from slightly crystalline to highly crystalline as the HT temperature is increased, with HT time constant at 4 h. First of all, the peak positions of thio-LISICON III analog do not change much for HT below 360 °C. In the case of HT at 480 °C (Fig. 5(c)) however, we not only see changes of crystallinity but also a negative shift of peaks are observed, which may be indicative of significant structural change. By comparison to the conductivities of PHT samples below 360 °C, we can say there is a close relation between the degree of crystallinity and conductivity, with conductivity decreasing with increased crystallinity with one exception of HT at 360 °C for 4 h. We attribute this decrease in conductivity to the changing intergranular resistance with crystallization of the material [25]. Presumably as we heat treat materials, the crystal growth or phase change induces grain boundary reconstruction towards a structure with higher activation energy and therefore higher resistance. Fig. 5(b) depicts the progression of HT of ABM powders at a constant temperature of 360 °C but for increasing HT times of 1, 2, and 4 h. We see a largely increasing degree of crystallinity with increasing HT time, but do not observe the same relationship as that of increasing temperature and constant time that we do with conductivity. In the case of increasing time at constant temperature (Fig. 5(b), 360 °C) we see an initial decrease in conductivity with increased crystallinity, but then observe an increase in conductivity when heat-treated to the maximum time of 4 h. We attribute this rise in conductivity to the completion of reaction in the PHT pellets. We observed color gradients within broken PHT pellets for lower times, but a consistent color throughout when heat-treated for 4 h. Because the temperature is highest on the outside of the pellet, the crystallization works inwards over time when held at a high temperature. Another explanation for the material gradient we observed could be due to the semi-rapid cooling the samples undergo after HT. By placing the PHT pellets on a cooling rack we have essentially quenched the material of which process could be responsible for the amorphous structure we see for the sample heat-treated to 480 °C for 1 h (Fig. 5(c)).

Fig. 6(a) shows the typical charge–discharge voltage profiles of $LiCoO_2$/Li cells using $Li_{4-x}Ge_{1-x}P_xS_{2(1+x)}Se_{2(1-x)}$ ($x = 0.95$, heat-treated at 480 °C for 1 h). Table 3 summarizes the electrochemical performance of ABM and heat-treated samples. The columbic efficiency for the first cycle of all samples is poor, but rapidly increases to almost unity by the 10th cycle. The low coulombic efficiency

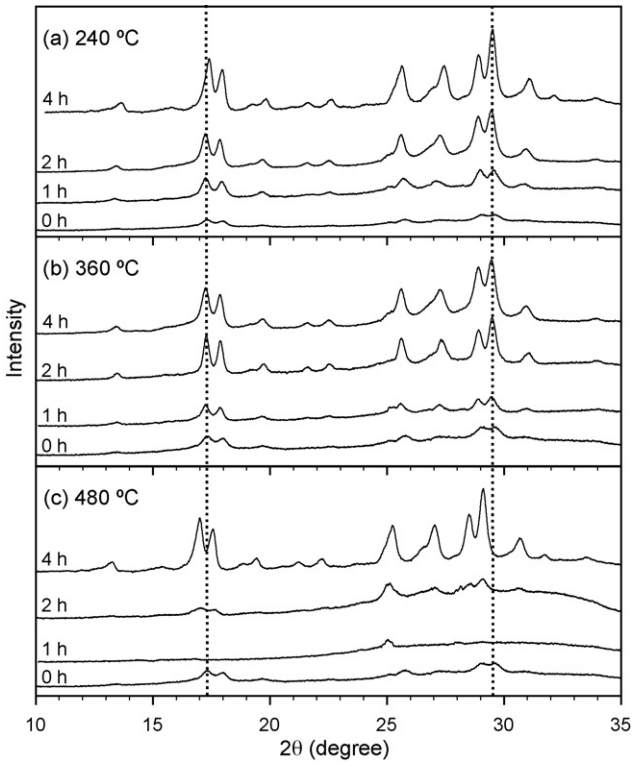

Fig. 5. XRD patterns of ABM and PHT series of $Li_{4-x}Ge_{1-x}P_xS_{2(1+x)}Se_{2(1-x)}$ with $x = 0.95$ heat-treated at (a) 240 °C, (b) 360 °C, and (c) 480 °C. Heating time is indicated on the left for each pattern.

Table 3
Electrochemical performance of $LiCoO_2/Li_{4-x}Ge_{1-x}P_{2(1+x)}S_{2(1-x)}$ with $x = 0.95$/Li cells.

Heat treatment		Capacity/mA h g^{-1}				
Temperature/°C	Time/h	1st		2nd		10th
		Charge	Discharge	Charge	Discharge	Discharge
ABM		141	33	94	63	17
240	4	126	46	103	82	39
360	1	138	60	123	96	29
360	2	154	53	113	88	41
360	4	162	60	122	96	38
480	1	136	58	115	95	62
480	2	124	53	112	89	34
480	4	136	58	115	95	33

mainly comes from a sloping plateau ('#') between 2.8 and 3.9 V indicates that a severe side reaction takes place on first charge process, which is also the case for all other cells using ABM and heat-treated SEs. We use differential capacity curves in Fig. 6(b) to show the differences in degradation of PHT materials. The $LiCoO_2$ should ideally create a charge reaction voltage plateau at 3.93 V and a discharge reaction plateau at 3.90 V which varies with dependence on electrolyte material and inconsistencies within a cell. Another noticeable theme in Fig. 6(b) is the progression of reaction voltage away from ideal. This behavior could be the result of contact between the oxide based cathode material and the sulfide based electrolyte material that creates a large chemical potential difference that should make Li^+ ions transfer from the sulfide electrolytes to the oxide electrodes. The space-charge layer in the sulfide electrolyte will be far more developed in contact with a mixed-conduction oxide such as $LiCoO_2$, rather than an ion-conducting oxide. When the sulfide and oxide ion-conducting species are in contact, the transfer of Li^+ ions forms a space-charge layer in both materials. With an electron conducting oxide (mixed conductor) the space-charge layer on the oxide side of the interface will vanish due to the electronic conduction, resolving the concentration gradient of Li^+ ions. Consequently, Li^+ ions will also transfer from the sulfide in order to reach equilibrium, further developing the space-charge layer on the sulfide side resulting in a very large interfacial resistance [26]. It is also obvious that the specific capacity decreases with increased cycling which may also be due to a charge-layer build up. A reaction at the interface of SE and active material may be creating a resistance barrier that causes the reaction voltage to shift towards a larger polarization. We speculate that under applied current, the lithium in the SE within the composite as well as at the electrolyte/composite interface may be undergoing lithiation and delithiation. It is possible that a lithium deficiency in the SE may be the cause of lithium trapping in the composite electrode, and be responsible for the enormous side reaction on the first cycle. Such a process could result in a number of inconsistencies that would result in degradation due to stress, lithium trapping, or charge layer build up. We also consider that the poor discharge efficiency could be the result of Li corrosion in contact with the SE. A reaction between the interface of the SE and the Li metal could also be responsible for a charge-layer build up. For all SE listed in Table 3, we found the sample heat-treated at 480 °C for 1 h shows the best performance; the smallest side reaction and the least capacity fade. Interestingly, the sample displaying the smallest first cycle side reaction and the best cycling performance is the only sample that has an amorphous structure.

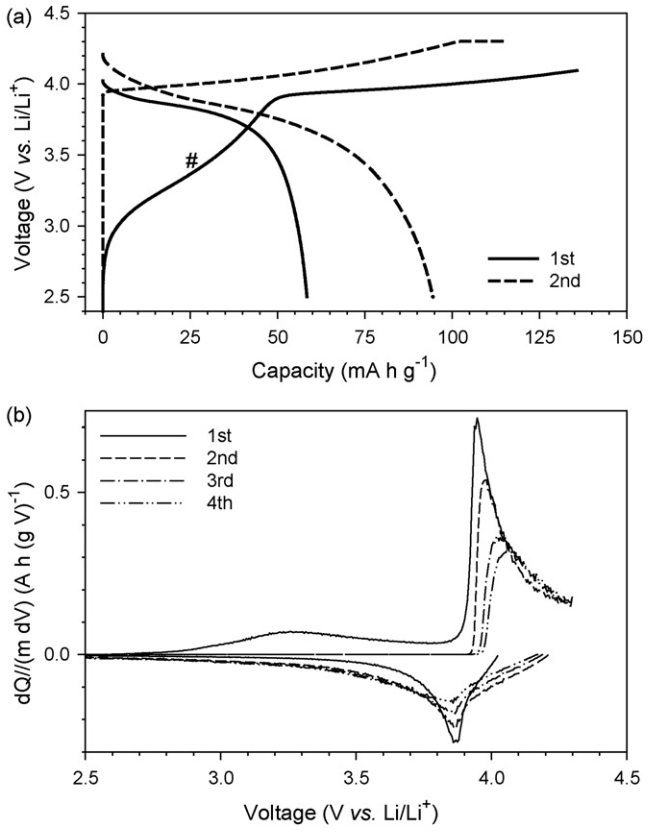

Fig. 6. (a) Charge–discharge and (b) differential charge–discharge capacity profiles for $Li_{4-x}Ge_{1-x}P_xS_{2(1+x)}Se_{2(1-x)}$ with $x = 0.95$ heat-treated at 480 °C for 1 h.

In spite of the achievement of extremely high bulk conductivities comparable to that of liquid electrolytes, we can conclude that the inferior capabilities of all-solid-state cells lie with interfacial discontinuities and reactions as well as chemical instability [26]. To improve the performance of all-solid-state batteries it is necessary to reduce resistances, in particular to improve the interface between electrodes and electrolytes to engender lower interfacial resistance [27–29].

4. Conclusion

Glass–ceramic and glass Li_2S–$GeSe_2$–P_2S_5 ($Li_{4-x}Ge_{1-x}P_xS_{2(1+x)}Se_{2(1-x)}$) electrolytes with various compositions from $x = 0.55$ to $x = 1.00$ were prepared by a simple SSBM process. The Li_2S–$GeSe_2$–P_2S_5 showed high conductivities of maximum 1.4×10^{-3} S cm^{-1} for $x = 0.95$ in $Li_{4-x}Ge_{1-x}P_xS_{2(1+x)}Se_{2(1-x)}$. Structural analysis showed that inclusion of $GeSe_2$ leads to the increased lattice followed by occurrence of new phase. All-solid-state $LiCoO_2$/Li cells using Li_2S–$GeSe_2$–P_2S_5 system showed a high specific capacity of over 100 mAh g^{-1} for the second cycle. HT of the ABM resulted in lower overall conductivities but better cycling performance and electrochemical stability. Especially, the sample heat-treated at 480 °C at 1 h for $Li_{4-x}Ge_{1-x}P_xS_{2(1+x)}Se_{2(1-x)}$ with $x = 0.95$ resulted in an amorphous structure that exhibited the best

performance among all samples. With the observation of relatively high conductivities comparable to that of liquid electrolytes, we can conclude that the inferior capabilities of all-solid-state cells lie with interfacial reactions and chemical instabilities.

Acknowledgments

This work has been supported by DARPA/DSO. Dr. Yoon Seok Jung acknowledges the Korea Research Foundation Grant funded by the Korean Government [KRF-2008-357-D00066].

References

[1] A. Hayashi, S. Hama, F. Mizuno, K. Tadanaga, T. Minami, M. Tatsumisago, Solid State Ionics 175 (2004) 683.
[2] A. Hayashi, S. Hama, T. Minami, M. Tatsumisago, Electrochem. Commun. 5 (2003) 111.
[3] N. Ohta, K. Takada, I. Sakaguchi, L. Zhang, R. Ma, K. Fukuda, M. Osada, T. Sasaki, Electrochem. Commun. 9 (2007) 1486.
[4] Y. Hashimoto, N. Machida, T. Shigematsu, Solid State Ionics 175 (2004) 177.
[5] K. Takada, T. Inada, A. Kajiyama, M. Kouguchi, H. Sasaki, S. Kondo, Y. Michiue, S. Nakano, M. Tabuchi, M. Watanabe, Solid State Ionics 172 (2004) 25.
[6] K. Takada, T. Inada, A. Kajiyama, H. Sasaki, S. Kondo, M. Watanabe, M. Murayama, R. Kanno, Solid State Ionics 158 (2003) 269.
[7] N. Machida, H. Yamamoto, S. Asano, T. Shigematsu, Solid State Ionics 176 (2005) 473.
[8] N. Machida, H. Maeda, H. Peng, T. Shigematsu, J. Electrochem. Soc. 149 (2002) A688.
[9] H. Kitaura, A. Hayashi, K. Tadanaga, M. Tatsumisago, J. Power Sources 189 (2005) 145.
[10] F. Mizuno, A. Hayashi, K. Tadanaga, M. Tatsumisago, Solid State Ionics 177 (2006) 2731.
[11] M. Tatsumisago, Solid State Ionics 175 (2004) 13.
[12] S. Kondo, K. Takada, Y. Yamamura, Solid State Ionics 53 (1992) 1183.
[13] F. Mizuno, A. Hama, A. Hayashi, K. Tadanaga, T. Minami, M. Tatsumisago, Chem. Lett. 31 (2002) 1244.
[14] A. Hayashi, S. Hama, H. Morimoto, M. Tatsumisago, T. Minami, J. Am. Ceram. Soc. 84 (2001) 477.
[15] H. Yamamoto, N. Machida, T. Shigematsu, Solid State Ionics 175 (2004) 707.
[16] M. Tatsumisago, F. Mizuno, A. Hayashi, J. Power Sources 159 (2006) 193.
[17] F. Mizuno, A. Hayashi, K. Tadanaga, M. Tatsumisago, Adv. Mater. 17 (2005) 918.
[18] A. Sakuda, H. Kitaura, A. Hayashi, K. Tadanaga, M. Tatsumisago, J. Power Sources 189 (2009) 527.
[19] R. Kanno, M. Murayama, J. Electrochem. Soc. 148 (2001) A742.
[20] J. Trevey, J.S. Jang, Y.S. Jung, C. Stoldt, S. Lee, Electrochem. Commun. 11 (2009) 1830.
[21] F. Mizuno, A. Hayashi, K. Tadanaga, M. Tatsumisago, Solid State Ionics 177 (2006) 2721.
[22] M. Tatsumisago, A. Hayashi, J. Non-Cryst. Solids 354 (2008) 1411.
[23] K. Minami, F. Mizuno, A. Hayashi, M. Tatsumisago, J. Non-Cryst. Solids 354 (2008) 370.
[24] K. Minami, F. Mizuno, A. Hayashi, M. Tatsumisago, Solid State Ionics 178 (2007) 837.
[25] Y. Kim, S. Martin, Solid State Ionics 177 (2006) 2881.
[26] N. Ohta, K. Takada, L. Zhang, R. Ma, M. Osada, T. Sasaki, Adv. Mater. 18 (2006) 2226.
[27] A. Sakuda, H. Kitaura, A. Hayashi, K. Tadanaga, M. Tatsumisago, J. Electrochem. Soc. 156 (2009) A27.
[28] F. Mizuno, A. Hayashi, K. Tadanaga, T. Minami, M. Tatsumisago, J. Power Sources 124 (2003) 170.
[29] K. Takada, N. Ohta, L. Zhang, K. Fukuda, I. Sakaguchi, R. Ma, M. Osada, T. Sasaki, Solid State Ionics 179 (2008) 1333.